







# Exploring potential for semiconductor to quantum anomalous Hall insulator transitions via substrate-induced structural modifications in $\text{Ti}_3\text{Se}_4$ monolayers

Zhipeng Song<sup>1,§</sup>, Haixia Cheng<sup>2,6,§</sup>, Yun Cao<sup>1</sup>, Qi Zheng<sup>1</sup>, Yurou Guan<sup>2</sup>, Chen Liu<sup>3</sup>, Jierui Huang<sup>1</sup>, Li Huang<sup>1</sup>, Jiaou Wang<sup>3</sup>, Hui Guo<sup>1</sup>, Guangchao Chen<sup>1</sup>, Chengmin Shen<sup>1</sup>, Shixuan Du<sup>1,4,5</sup>, Hongliang Lu<sup>1,5</sup>  , Wei Ji<sup>1,5</sup>  , Xiao Lin<sup>1,5</sup>  , and Hong-Jun Gao<sup>1,4,5</sup>

<sup>1</sup> University of Chinese Academy of Sciences and Institute of Physics, Chinese Academy of Sciences, Beijing 100190, China

<sup>2</sup> Beijing Key Laboratory of Optoelectronic Functional Materials & Micro-Nano Devices, School of Physics, Renmin University of China, Beijing 100872, China


<sup>3</sup> Institute of High Energy Physics, Chinese Academy of Sciences, Beijing 100049, China

<sup>4</sup> Songshan Lake Materials Laboratory, Dongguan 523808, China

<sup>5</sup> CAS Center for Excellence in Topological Quantum Computation, University of Chinese Academy of Sciences, Beijing 100190, China

<sup>6</sup> Material Digital R & D Center, China Iron & Steel Research Institute Group, Beijing 100081, China

<sup>§</sup> Zhipeng Song and Haixia Cheng contributed equally to this work.

 Cite this article: *Nano Research*, 2025, 18, 94907123. <https://doi.org/10.26599/NR.2025.94907123>

**ABSTRACT:** The quantum anomalous Hall (QAH) effect in two-dimensional (2D) topological materials has attracted widespread attention due to its potential for dissipationless chiral edge transport without an external magnetic field, which is highly promising for low-power electronic applications. However, identifying materials that exhibit these properties remains particularly challenging, as only a limited number of such materials are known, raising the intriguing question of whether it is possible to induce the QAH effect in materials with ordinary properties through structural modifications. In this work, we grow an unreported 2D titanium selenide ( $\text{Ti}_3\text{Se}_4$ ) on a Cu(111) substrate using molecular beam epitaxy. Low-energy electron diffraction and scanning tunneling microscopy characterizations reveal a  $\sqrt{7} \times \sqrt{7}$  brick-like structure. First-principles calculations and X-ray photoelectron spectroscopy measurements confirm its composition to be  $\text{Ti}_3\text{Se}_4$ . Our calculations further demonstrate that monolayer  $\text{Ti}_3\text{Se}_4$ , in its grown form on Cu(111), has the potential to host the QAH effect. Interestingly, when we examine its freestanding form, the monolayer transitions from a QAH insulator candidate into a conventional semiconductor, despite only minor differences in their atomic structures. This transition enlightens us that subtle lattice adjustments can induce a transition from semiconductor to QAH properties in freestanding  $\text{Ti}_3\text{Se}_4$ . This discovery provides a potential route to engineering practical materials that may exhibit the QAH effect.

**KEYWORDS:** quantum anomalous Hall (QAH) effect, monolayer  $\text{Ti}_3\text{Se}_4$ , structural modifications, semiconductor, molecular beam epitaxy

## 1 Introduction

Topological insulators, distinguished by their topologically nontrivial band structures, have attracted significant research

interest due to their unique physical properties and potential applications [1–7]. Among these, the quantum anomalous Hall (QAH) effect is particularly intriguing. It features topologically protected quantized Hall resistance and zero longitudinal resistance without an external magnetic field [3, 8]. Bulk topological insulators possess a band gap, while their surfaces exhibit gapless Dirac states protected by time-reversal symmetry. However, introducing ferromagnetic order through magnetic doping breaks this time-reversal symmetry, leading to the opening of a gap at the Dirac point in the surface states [9]. When the Fermi level falls within this

Received: August 27, 2024; Revised: October 17, 2024

Accepted: November 7, 2024

 Address correspondence to Hongliang Lu, [luhl@ucas.ac.cn](mailto:luhl@ucas.ac.cn); Wei Ji, [wji@ruc.edu.cn](mailto:wji@ruc.edu.cn); Xiao Lin, [xlin@ucas.ac.cn](mailto:xlin@ucas.ac.cn)

exchange gap, a chiral edge mode emerges, giving rise to a topologically nontrivial electronic structure that manifests the QAH effect [10–12]. Materials exhibiting this effect hold significant potential for future low-power electronic applications [8].

Despite their importance, materials that exhibit the QAH effect are exceedingly rare. The pioneering experimental observation of the QAH effect was in magnetically doped  $(\text{Bi,Sb})_2(\text{Se,Te})_3$  [13–19]. Finding intrinsic magnetic topological insulators is considered to be a crucial strategy for enhancing the critical temperature of the QAH effect.  $\text{MnBi}_2\text{Te}_4$  is one such material, where the QAH effect is observed at 1.4 K without a magnetic field and 6.5 K with a magnetic field in a five-septuple-layer specimen [11]. The QAH effect was also observed in multilayer graphene [20–23] and AB-stacked  $\text{MoTe}_2/\text{WSe}_2$  moiré heterobilayers [24]. However, the practical application of the QAH effect remains limited because of the instability of these materials in air and requirement for extremely low temperatures. Therefore, there is an urgent need to develop other methodologies to discover materials that exhibit the QAH effect that are suitable for practical applications.

In this work, we report a strategy to grow titanium selenides using molecular beam epitaxy (MBE), enabling fabrication of monolayer  $\text{Ti}_3\text{Se}_4$ , an unreported 2D material, on a Cu(111) substrate. Using a combination of scanning tunneling microscopy (STM), low-energy electron diffraction (LEED), X-ray photoelectron spectroscopy (XPS) and density functional theory (DFT) calculations, we characterized the brick-like atomic structure and the 3:4 composition of this material. Our first-principles calculations show that, while free-standing  $\text{Ti}_3\text{Se}_4$  is a semiconductor, the  $\text{Ti}_3\text{Se}_4$  monolayer in the form grown on the Cu(111) substrate has the potential to exhibit QAH effect. Furthermore, although the QAH effect has been demonstrated in thin films or multi-layer materials, no studies have yet shown this effect in a monolayer where atoms are connected by covalent bonds.

## 2 Experimental section and calculation

### 2.1 Sample preparation

Monolayer  $\text{Ti}_3\text{Se}_4$  on Cu(111) substrate was grown in an ultra-high vacuum molecular beam epitaxy system with a base pressure lower than  $5 \times 10^{-10}$  mbar. The atomically clean Cu(111) surface was obtained by cycles of argon-ion sputtering and annealing until clean surface was confirmed in STM images and sharp LEED patterns. Firstly, The high-purity Se (99.99%) was deposited to the clean Cu(111) substrate from Knudsen cell while the substrate was kept at 650 K to form the non-hole monolayer CuSe. Then Ti (99.9%) was deposited from electron-beam evaporators, and the substrate was kept at 650 K. Finally monolayer  $\text{Ti}_3\text{Se}_4$  can be formed on the Cu(111) surface. After several experiments, we found that the effective way to fabricate this special 2D material  $\text{Ti}_3\text{Se}_4$  is by using CuSe as a precursor. All the characterizations were done in ultra-high vacuum environment by using *in-situ* transfer technique. The LEED and STM characterizations were performed at a base pressure of  $\sim 3 \times 10^{-10}$  mbar. LEED patterns were carried out with a commercial high-resolution instrument and the electron energy used in experiment was 66 eV. STM measurements were performed in the constant-current mode. *In-situ* XPS measurements were performed at the Beijing Synchrotron Radiation Facility with a hemispherical energy analyzer.

### 2.2 Calculation details

Spin-polarized DFT calculations were performed using the projector augmented wave method [25, 26] with the Perdew–Burke–Ernzerhof exchange correlation functional as implemented in the Vienna *ab-initio* simulation package [27, 28]. The density-dependent-dispersion-corrected PBE functional (PBE-dDsC) method was chosen for the van der Waals correction [29–31]. A kinetic energy cutoff of 500 eV for the plane-wave basis set was used. The Brillouin zone was sampled using a uniform  $\Gamma$ -centered  $9 \times 9 \times 1$  ( $15 \times 15 \times 1$ ) Monkhorst-pack  $k$ -mesh for structural relaxations (electronic structure calculations) of monolayer  $\text{Ti}_3\text{Se}_4$ . Spin-orbit coupling (SOC) was considered in electronic structure calculations for monolayer  $\text{Ti}_3\text{Se}_4$ . The  $\text{Ti}_3\text{Se}_4/\text{Cu}(111)$  interface was modelled using a  $\text{Ti}_3\text{Se}_4$  monolayer and five layers of the Cu(111) plane with two fixed bottom layers. A vacuum layer of  $\sim 15$  Å was used to eliminate interactions between periodic layers. Fixing the lattice constant identical to the Cu substrate, atomic positions were relaxed until the residual force on each atom was less than 0.01 eV/Å. The edge states of monolayer  $\text{Ti}_3\text{Se}_4$  were calculated by means of maximally localized Wannier functions implemented in the WANNIER 90 package.

## 3 Results and discussion

### 3.1 Structural characterization of monolayer $\text{Ti}_3\text{Se}_4$ grown on Cu(111) substrate

The ratio of Ti and Se in common titanium selenides is 1:2, and synthesizing a 3:4 phase is a challenging task due to the difficulty in controlling the ratio. Here, we used a monolayer CuSe/Cu(111) as a template to determine the amount of Se, and then only needed to control the amount of Ti to obtain  $\text{Ti}_3\text{Se}_4$ . The growth process is schematically shown in Fig. 1(a). High-purity Se was evaporated onto the Cu(111) surface to form monolayer CuSe [32]. The LEED pattern in Fig. S1(a) in the Electronic Supplementary Material (ESM) shows hexagonal crystal structure and the STM image in Fig. S1(b) in the ESM shows atomically flat surface with 1D moiré pattern, which indicate the formation of CuSe on Cu(111) substrate [32]. Then Ti atoms were deposited on the CuSe/Cu(111) surface, which changed the LEED pattern to that shown in Fig. 1(b). The outer six diffraction spots highlighted by the white circles originate from the Cu(111) substrate with six-fold symmetry and the other distinct diffraction spots are assigned to the new material. For clarity, we sketched a simulated diffraction pattern of the sample in reciprocal space in Fig. 1(c), where each group of spots in different colors are derived from different domains and one group of the reciprocal vectors of such spots are depicted by the red arrows. The lattice of this 2D material in real space is schematically shown in Fig. 1(d), which is a  $\sqrt{7} \times \sqrt{7}$  structure with respect to the Cu(111) substrate.

Figure 2(a) presents a medium-scale STM image of  $\text{Ti}_3\text{Se}_4$ , while Fig. 2(b) displays a high-resolution STM image of this new 2D material, which exhibits a brick-like morphology. The primitive cell of crystal lattice is marked by a red rhombus, which shows an angle of approximately  $100^\circ$  between vectors  $a$  and  $b$ . The lattice constants of this primitive cell are about  $a = 6.95$  Å,  $b = 7.08$  Å. Figure S2(a) in the ESM shows a representative large-scale STM image, while Fig. S2(b) in the ESM shows the morphology covering

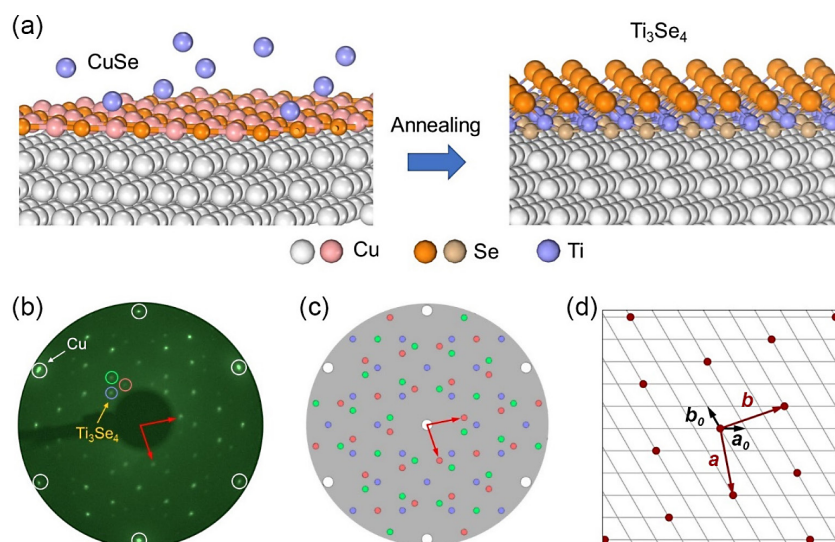


**Figure 1** The growth process and the structure of Ti<sub>3</sub>Se<sub>4</sub>. (a) Schematic illustrations of the growth process of Ti<sub>3</sub>Se<sub>4</sub>. (b) LEED pattern of Ti<sub>3</sub>Se<sub>4</sub> formed on Cu(111) surface. The white circles indicate the diffraction spots of Cu(111) substrate and the additional diffraction spots are ascribed to the Ti<sub>3</sub>Se<sub>4</sub>. (c) Sketch of the diffraction spots shown in (b), which are generated by three domains as represented in different colors. (d) Schematic diagram of Ti<sub>3</sub>Se<sub>4</sub> lattice in real space, corresponding to one set of the diffraction spots (the red spots) in (c). The dark red and black arrows show the lattice vectors of the monolayer Ti<sub>3</sub>Se<sub>4</sub> and the Cu(111) substrate, respectively.

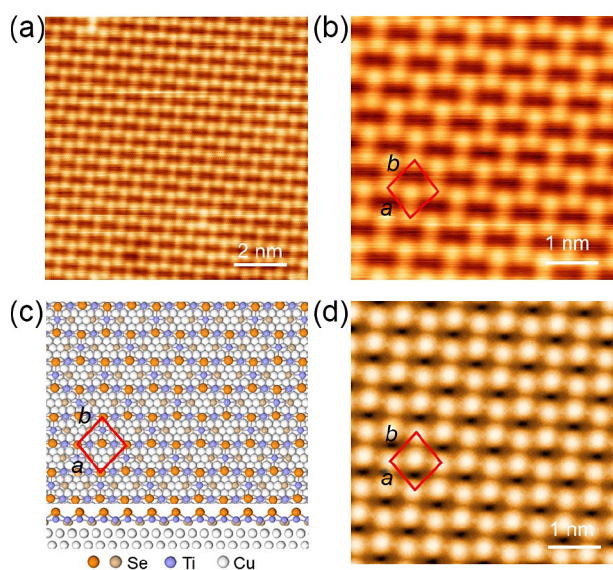


**Figure 2** STM images and atomic configuration of monolayer Ti<sub>3</sub>Se<sub>4</sub>. (a) Medium-scale STM image of Ti<sub>3</sub>Se<sub>4</sub>. (b) High-resolution STM image of monolayer Ti<sub>3</sub>Se<sub>4</sub> ( $V_S = -0.7$  V,  $I_t = 50$  pA,  $T = 4.5$  K). (c) Top and side view of the atomic model of monolayer Ti<sub>3</sub>Se<sub>4</sub> on Cu(111) substrate optimized by DFT calculation. (d) STM simulation of monolayer Ti<sub>3</sub>Se<sub>4</sub> on Cu(111) substrate with  $V_S = -0.7$  V.

an edge of this material on Cu(111), showing that its height of approximately 0.47 nm (Fig. S2(c) in the ESM).

### 3.2 Structural confirmation of monolayer Ti<sub>3</sub>Se<sub>4</sub>

To confirm the structure of this 2D material, we constructed an atomic model of monolayer titanium selenide with a chemical formula of Ti<sub>3</sub>Se<sub>4</sub> according to the experimentally obtained lattice constants. The optimized atomic structure of Ti<sub>3</sub>Se<sub>4</sub>/Cu(111) is shown in Fig. 2(c), in which the primitive cell was marked by a red rhombus. We compared experimental and simulated STM images, both acquired at a bias voltage of  $-0.7$  V. These images are highly

consistent in terms of surface morphology and lattice constants (Figs. 2(b) and 2(d)). This consistency strongly supports that the experimentally fabricated 2D monolayer is indeed Ti<sub>3</sub>Se<sub>4</sub>, as depicted in Fig. 2(c). Further characterization of monolayer Ti<sub>3</sub>Se<sub>4</sub> revealed that its STM morphology image varies under different biases. As shown in Figs. S3(a)–S3(c) in the ESM, the STM images show a brick-like morphology when the absolute bias value ( $|V|$ ) exceeds 0.4 V, whereas a rectangular morphology is observed when the absolute bias value is below 0.4 V. The corresponding STM simulation images, presented in Figs. S3(d)–S3(f) in the ESM, are in good agreement with the experimental results. To verify the actual surface structure, we conducted atomic force microscopy (AFM) characterization. The results, shown in Fig. S4 in the ESM, are well consistent with the LEED pattern, indicating that the brick-like morphology is the inherent structure of monolayer Ti<sub>3</sub>Se<sub>4</sub>.

High-resolution XPS measurements were subsequently conducted to further verify the chemical composition of the sample. Figure S5(a) in the ESM shows the Ti 2p photoelectron spectrum which reflects two chemical states of the titanium. The two blue peaks are located at 454.3 and 460.4 eV, while the other two red peaks are located at 455.9 and 461.8 eV, respectively. Clearly, the valence state of titanium here is inconsistent with tetravalent titanium [33, 34]. If we compare the peaks of Ti 2p<sub>3/2</sub> (454.3 and 455.9 eV) with the standard XPS spectra [35], we find the oxidation states of Ti in this material are +2 and +3. The Se 3d<sub>3/2</sub> and 3d<sub>5/2</sub> peaks are located at 55.1 and 54.2 eV, respectively, as shown in Fig. S5(b) in the ESM, indicating the chemical state of Se<sup>2-</sup> [35]. Therefore, the XPS measurement corroborate that this new 2D material is Ti<sub>3</sub>Se<sub>4</sub>.

### 3.3 Band structures of the monolayer Ti<sub>3</sub>Se<sub>4</sub>

We next examined the potential applications of the as-fabricated Ti<sub>3</sub>Se<sub>4</sub> in electronic devices by calculating its band structures using the Ti<sub>3</sub>Se<sub>4</sub> monolayer structure directly detached from the fully relaxed Ti<sub>3</sub>Se<sub>4</sub>/Cu(111) interface (Figs. 2(c) and 3(a)). This model excluded the influence of the substrate, standing out the intrinsic electronic properties of the Ti<sub>3</sub>Se<sub>4</sub> monolayer. Figure 3(b) shows the



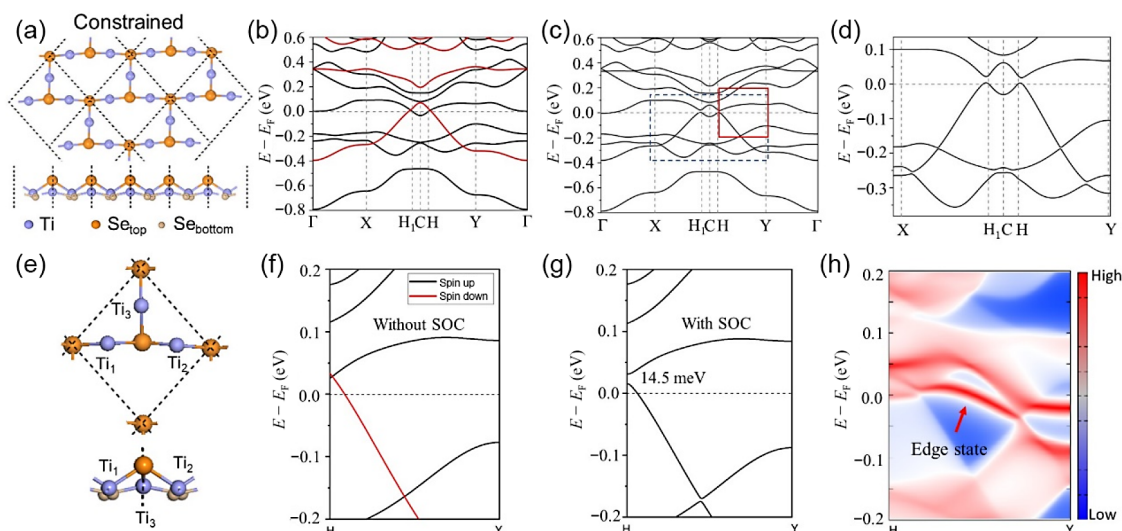


**Figure 3** Calculated band structures of the constrained  $\text{Ti}_3\text{Se}_4$ . (a) The atomic model of the constrained  $\text{Ti}_3\text{Se}_4$  by Cu(111) substrate. In the top panel, the bottom Se atoms are not depicted. (b) and (c) Calculated band structures of constrained  $\text{Ti}_3\text{Se}_4$  without and with SOC, respectively. (d) Zoom-in band structures in the blue dashed rectangle in (c), showing an obvious SOC-induced energy gap near the Fermi level. (e) The primary source of magnetic moment in constrained monolayer  $\text{Ti}_3\text{Se}_4$  arises from Ti atoms. (f) and (g) The band structures of constrained  $\text{Ti}_3\text{Se}_4$  along the H-Y direction without and with SOC, respectively, and (g) corresponds to the red rectangle in (c). (h) Edge state of the constrained  $\text{Ti}_3\text{Se}_4$  denoted by the red arrow.

calculated band structures of the brick-like  $\text{Ti}_3\text{Se}_4$  monolayer without SOC. The black and red curves represent the electronic bands with spin-up and -down components, respectively, revealing that the spin-up and spin-down bands cross near the Fermi level, close to points  $H_1$  and H in the first Brillouin zone. Including SOC in the calculations results in energy gaps at the crossing points of these two bands, leading to band inversion as shown in Figs. 3(c) and 3(d). Figure 3(e) highlights the primary source of magnetic moment in this constrained monolayer  $\text{Ti}_3\text{Se}_4$  arising from Ti atoms. For clarity, magnified band structures of  $\text{Ti}_3\text{Se}_4$  along the H-Y direction, both without and with SOC, are presented in Figs. 3(f) and 3(g), respectively. A gap of 14.5 meV is clearly identified above the Fermi level, close to the H point. Remarkably, this material exhibits a large magnetic moment ( $2.13 \mu_B/\text{cell}$ ) primarily resulted from the titanium atoms, as shown in Fig. 3(e). Considering the gap opening after SOC and the appearance of the large magnetic moment, we anticipate that this brick-like monolayer  $\text{Ti}_3\text{Se}_4$  is a topological material capable of exhibiting the QAH effect. To further verify the QAH effect, we calculated the edge state of the brick-like  $\text{Ti}_3\text{Se}_4$  monolayer. Figure 3(h) shows a detailed band structure diagram, clearly highlighting the edge state marked by the red arrow. The presence of the edge state, in addition to the SOC-induced gap, confirms that this monolayer satisfies the criteria of exhibiting the QAH effect.

We next investigated the thermal stability and the corresponding electronic structures of the fully relaxed free-standing  $\text{Ti}_3\text{Se}_4$  monolayer. The freestanding  $\text{Ti}_3\text{Se}_4$  is found to be stable and exhibits only minor structural differences compared to the monolayer derived from the  $\text{Ti}_3\text{Se}_4/\text{Cu}(111)$  interface, as shown in Fig. 4(a). Specifically, a set of Se atoms shift inward, forming a concave "brick" structure, while all Ti atoms shift upwards with the Ti atoms on the long side of the brick shifting further. These in-plane structural changes lead to lattice constants  $a = 5.87 \text{ \AA}$ ,  $b = 5.87 \text{ \AA}$ , and  $\theta = 99.8^\circ$ . Figure 4(b) depicts the Brillouin zone of monolayer  $\text{Ti}_3\text{Se}_4$ . Figure 4(c) shows the calculated band structure of freestanding

monolayer  $\text{Ti}_3\text{Se}_4$  without SOC, revealing spin degenerate bands and a clear gap around the Fermi level. This band structure feature indicates that the freestanding  $\text{Ti}_3\text{Se}_4$  monolayer is a semiconductor with a sizable band gap ( $\sim 0.14 \text{ eV}$ ). Including SOC results in a slight band splitting, enlarging the band gap from 0.14 to 0.15 eV, as shown in Fig. 4(d). This small band gap suggests potential applications of this material in mid-infrared electronic devices.

## 4 Discussion

The QAH effect has vast potential for applications in quantum computing and advanced electronic devices. However, its practical use is hindered by the limited number of materials that exhibit the QAH effect, their instability in atmospheric conditions, and the need for ultra-low operational temperatures. Our computational findings offer a promising solution. We have shown that the presence of the substrate lifts the out-of-plane inversion symmetry, accompanied by minor lattice and structural adjustments, in the semiconducting  $\text{Ti}_3\text{Se}_4$  monolayer, which can induce the QAH effect. This discovery suggests that similar modifications could be applied to air-stable 2D materials. In other words, the QAH effect could potentially be induced by slightly altering the atomic structure, which could be utilized either by applying mechanical stress (stretching, compressing, or bending) or temperature-induced structural phase transitions. Although these methods may not always achieve the QAH effect, they present a more efficient and practical approach compared to synthesizing new materials. Based on this example, we can further perform lattice tuning on other stable 2D semiconductor materials to investigate whether the QAH effect can emerge. We believe that sustained research and development in this direction can overcome existing limitations and significantly promote future applications of the QAH effect.

## 5 Conclusions

In summary, we have successfully grown the  $\text{Ti}_3\text{Se}_4$  monolayer on



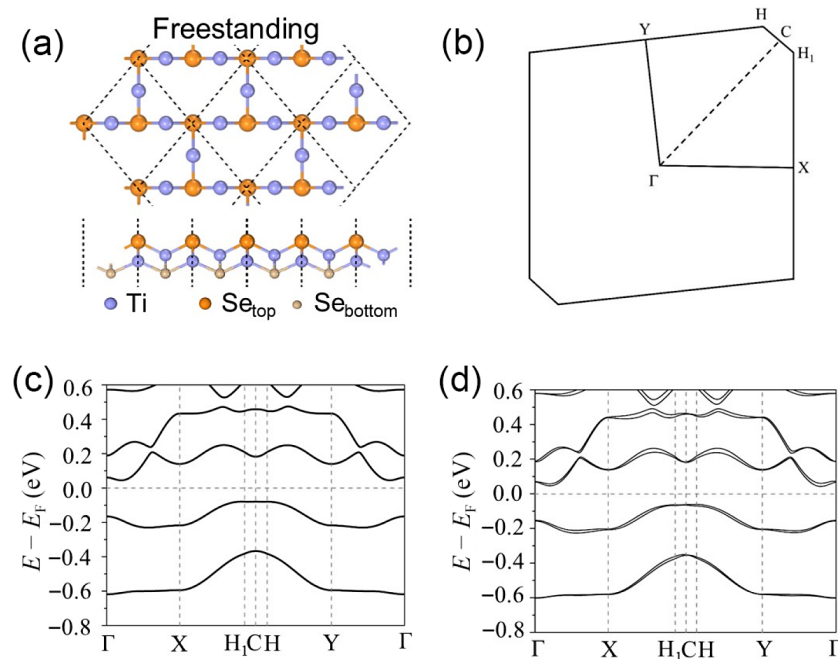


**Figure 4** Calculated band structures of the freestanding  $\text{Ti}_3\text{Se}_4$ . (a) The atomic model of freestanding  $\text{Ti}_3\text{Se}_4$ . In the top panel, the bottom Se atoms are not shown. (b) Brillouin zone of monolayer  $\text{Ti}_3\text{Se}_4$ . (c) and (d) Calculated band structures of the freestanding  $\text{Ti}_3\text{Se}_4$  without and with spin-orbit coupling (SOC), respectively.

the Cu(111) substrate using the MBE method. The LEED analysis indicates that this monolayer has a  $\sqrt{7} \times \sqrt{7}$  rhombus structure relative to the substrate. Our STM characterizations revealed a brick-like morphology. The structure of  $\text{Ti}_3\text{Se}_4$  is further confirmed by DFT calculations and XPS characterizations. Our DFT calculations also indicate that the freestanding  $\text{Ti}_3\text{Se}_4$  monolayer is a conventional semiconductor. However, when constrained, the monolayer exhibits a split in the original spin degeneracy, which has the potential to host the QAH effect. This significant change in properties results from slight shifts in atomic positions, making it feasible for experimental utilization. This work paves the way for using stable, well-known 2D materials to induce more intriguing electronic properties that are difficult to achieve in these materials.

**Electronic Supplementary Material:** Supplementary material (the structure characterization of CuSe, the measurement of the thickness of monolayer  $\text{Ti}_3\text{Se}_4$  on Cu(111), STM images of monolayer  $\text{Ti}_3\text{Se}_4$  under different biases, non-contact atomic force microscope image of monolayer  $\text{Ti}_3\text{Se}_4$ , XPS characterization of  $\text{Ti}_3\text{Se}_4$ ) is available in the online version of this article at <https://doi.org/10.26599/NR.2025.94907123>.

### Data availability

All data needed to support the conclusions in the paper are presented in the manuscript and the ESM. Additional data related to this paper may be requested from the corresponding author upon request.

### Acknowledgements

We acknowledge financial support from the National Key R&D Program of China (Nos. 2019YFA0308500 and 2018YFA0305800), the National Natural Science Foundation of China (Nos. 61925111, 61888102, 11974422, and U23A6015), CAS Project for Young

Scientists in Basic Research (No. YSBR-003), the Strategic Priority Research Program of Chinese Academy of Sciences (Nos. XDB28000000 and XDB30000000), the Fundamental Research Funds for the Central Universities provided to University of Chinese Academy of Sciences and to Renmin University of China (No. 22XNKJ30 (W. J.)), and the CAS Key Laboratory of Vacuum Physics. Calculations were performed at the Physics Lab of High-Performance Computing of Renmin University of China, Shanghai Supercomputer Center and Beijing Supercomputing Center.

### Declaration of competing interest

All the contributing authors report no conflict of interests in this work.

### Author contribution statement

Z. P. S.: Data curation, validation, writing manuscript. H. X. C.: Data curation, validation, writing manuscript. Y. C.: Data curation. Q. Z.: Data curation. Y. R. G.: Data curation. C. L.: Data curation. J. R. H.: Data curation. L. H.: Data curation. J. O. W.: Data curation. H. G.: Data curation. G. C. C.: Funding acquisition. C. M. S.: Data curation. S. X. D.: Funding acquisition. H. L. L.: Data curation, writing manuscript, funding acquisition. W. J.: Data curation, writing manuscript, funding acquisition. X. L.: Project administration, experimental design, writing manuscript, funding acquisition. H. J. G.: Project administration, funding acquisition. All the authors have approved the final manuscript.

### Use of AI statement

None.

### References

- [1] Hasan, M. Z.; Kane, C. L. Colloquium: Topological insulators. *Rev. Mod. Phys.* **2010**, *82*, 3045–3067.

- [2] Xu, Y.; Yan, B. H.; Zhang, H. J.; Wang, J.; Xu, G.; Tang, P. Z.; Duan, W. H.; Zhang, S. C. Large-Gap quantum spin hall insulators in thin films. *Phys. Rev. Lett.* **2013**, *111*, 136804.
- [3] Wang, C. X.; Zhu, X. G.; Nilsson, L.; Wen, J.; Wang, G.; Shan, X. Y.; Zhang, Q.; Zhang, S. L.; Jia, J. F.; Xue, Q. K. *In situ* Raman spectroscopy of topological insulator Bi<sub>2</sub>Te<sub>3</sub> films with varying thickness. *Nano Res.* **2013**, *6*, 688–692.
- [4] Yu, R.; Zhang, W.; Zhang, H. J.; Zhang, S. C.; Dai, X.; Fang, Z. Quantized anomalous hall effect in magnetic topological insulators. *Science* **2010**, *329*, 61–64.
- [5] Fu, L.; Kane, C. L. Topological insulators with inversion symmetry. *Phys. Rev. B* **2007**, *76*, 045302.
- [6] Ren, Z.; Taskin, A. A.; Sasaki, S.; Segawa, K.; Ando, Y. Large bulk resistivity and surface quantum oscillations in the topological insulator Bi<sub>2</sub>Te<sub>3</sub>Se. *Phys. Rev. B* **2010**, *82*, 241306.
- [7] Wang, J.; Li, H. D.; Chang, C. Z.; He, K.; Lee, J. S.; Lu, H. Z.; Sun, Y.; Ma, X. C.; Samarth, N.; Shen, S. Q. et al. Anomalous anisotropic magnetoresistance in topological insulator films. *Nano Res.* **2012**, *5*, 739–746.
- [8] Chang, C. Z.; Zhang, J. S.; Feng, X.; Shen, J.; Zhang, Z. C.; Guo, M. H.; Li, K.; Ou, Y. B.; Wei, P.; Wang, L. L. et al. Experimental observation of the quantum anomalous hall effect in a magnetic topological insulator. *Science* **2013**, *340*, 167–170.
- [9] Chen, Y. L.; Chu, J. H.; Analytis, J. G.; Liu, Z. K.; Igarashi, K.; Kuo, H. H.; Qi, X. L.; Mo, S. K.; Moore, R. G.; Lu, D. H. et al. Massive dirac fermion on the surface of a magnetically doped topological insulator. *Science* **2010**, *329*, 659–662.
- [10] Qi, X. L.; Hughes, T. L.; Zhang, S. C. Topological field theory of time-reversal invariant insulators. *Phys. Rev. B* **2008**, *78*, 195424.
- [11] Deng, Y. J.; Yu, Y. J.; Shi, M. Z.; Guo, Z. X.; Xu, Z. H.; Wang, J.; Chen, X. H.; Zhang, Y. B. Quantum anomalous hall effect in intrinsic magnetic topological insulator MnBi<sub>2</sub>Te<sub>4</sub>. *Science* **2020**, *367*, 895–900.
- [12] Liu, C. X.; Qi, X. L.; Dai, X.; Fang, Z.; Zhang, S. C. Quantum anomalous hall effect in Hg<sub>1-x</sub>Mn<sub>x</sub>Te quantum wells. *Phys. Rev. Lett.* **2008**, *101*, 146802.
- [13] Yue, C. M.; Xu, Y. F.; Song, Z. D.; Weng, H. M.; Lu, Y. M.; Fang, C.; Dai, X. Symmetry-enforced chiral hinge states and surface quantum anomalous hall effect in the magnetic axion insulator Bi<sub>2-x</sub>Sm<sub>x</sub>Se<sub>3</sub>. *Nat. Phys.* **2019**, *15*, 577–581.
- [14] Checkelsky, J. G.; Yoshimi, R.; Tsukazaki, A.; Takahashi, K. S.; Kozuka, Y.; Falson, J.; Kawasaki, M.; Tokura, Y. Trajectory of the anomalous hall effect towards the quantized state in a ferromagnetic topological insulator. *Nat. Phys.* **2014**, *10*, 731–736.
- [15] Chang, C. Z.; Zhao, W. W.; Kim, D. Y.; Zhang, H. J.; Assaf, B. A.; Heiman, D.; Zhang, S. C.; Liu, C. X.; Chan, M. H. W.; Moodera, J. S. High-precision realization of robust quantum anomalous hall state in a hard ferromagnetic topological insulator. *Nat. Mater.* **2015**, *14*, 473–477.
- [16] Wang, J.; Lian, B.; Zhang, H. J.; Xu, Y.; Zhang, S. C. Quantum anomalous hall effect with higher plateaus. *Phys. Rev. Lett.* **2013**, *111*, 136801.
- [17] Xiao, D.; Jiang, J.; Shin, J. H.; Wang, W. B.; Wang, F.; Zhao, Y. F.; Liu, C. X.; Wu, W. D.; Chan, M. H. W.; Samarth, N. et al. Realization of the axion insulator state in quantum anomalous hall sandwich heterostructures. *Phys. Rev. Lett.* **2018**, *120*, 056801.
- [18] Liu, W. Q.; West, D.; He, L.; Xu, Y. B.; Liu, J.; Wang, K. J.; Wang, Y.; van der Laan, G.; Zhang, R.; Zhang, S. B. et al. Atomic-scale magnetism of Cr-doped Bi<sub>2</sub>Se<sub>3</sub> thin film topological insulators. *ACS Nano* **2015**, *9*, 10237–10243.
- [19] Nan, J. L.; Liu, Y. Q.; Chao, D. Y.; Fang, Y. X.; Dong, S. J. Crystal defect engineering of Bi<sub>2</sub>Te<sub>3</sub> nanosheets by Ce doping for efficient electrocatalytic nitrogen reduction. *Nano Res.* **2023**, *16*, 6544–6551.
- [20] Geisenhof, F. R.; Winterer, F.; Seiler, A. M.; Lenz, J.; Xu, T. Y.; Zhang, F.; Weitz, R. T. Quantum anomalous hall octet driven by orbital magnetism in bilayer graphene. *Nature* **2021**, *598*, 53–58.
- [21] Serlin, M.; Tschirhart, C. L.; Polshyn, H.; Zhang, Y.; Zhu, J.; Watanabe, K.; Taniguchi, T.; Balents, L.; Young, A. F. Intrinsic quantized anomalous hall effect in a moiré heterostructure. *Science* **2020**, *367*, 900–903.
- [22] Polshyn, H.; Zhu, J.; Kumar, M. A.; Zhang, Y.; Yang, F.; Tschirhart, C. L.; Serlin, M.; Watanabe, K.; Taniguchi, T.; MacDonald, A. H. et al. Electrical switching of magnetic order in an orbital Chern insulator. *Nature* **2020**, *588*, 66–70.
- [23] Chen, G. R.; Sharpe, A. L.; Fox, E. J.; Zhang, Y. H.; Wang, S. X.; Jiang, L. L.; Lyu, B.; Li, H. Y.; Watanabe, K.; Taniguchi, T. et al. Tunable correlated Chern insulator and ferromagnetism in a moiré superlattice. *Nature* **2020**, *579*, 56–61.
- [24] Li, T. X.; Jiang, S. W.; Shen, B. W.; Zhang, Y.; Li, L. Z.; Tao, Z.; Devakul, T.; Watanabe, K.; Taniguchi, T.; Fu, L. et al. Quantum anomalous hall effect from intertwined moiré bands. *Nature* **2021**, *600*, 641–646.
- [25] Blöchl, P. E. Projector augmented-wave method. *Phys. Rev. B* **1994**, *50*, 17953–17979.
- [26] Kresse, G.; Joubert, D. From ultrasoft pseudopotentials to the projector augmented-wave method. *Phys. Rev. B* **1999**, *59*, 1758–1775.
- [27] Kresse, G.; Furthmüller, J. Efficient iterative schemes for *ab initio* total-energy calculations using a plane-wave basis set. *Phys. Rev. B* **1996**, *54*, 11169–11186.
- [28] Kresse, G.; Furthmüller, J. Efficiency of *ab-initio* total energy calculations for metals and semiconductors using a plane-wave basis set. *Comp. Mater. Sci.* **1996**, *6*, 15–50.
- [29] Klimeš, J.; Bowler, D. R.; Michaelides, A. Chemical accuracy for the van der Waals density functional. *J. Phys.: Condens. Matter* **2010**, *22*, 022201.
- [30] Dion, M.; Rydberg, H.; Schröder, E.; Langreth, D. C.; Lundqvist, B. I. Van der Waals density functional for general geometries. *Phys. Rev. Lett.* **2004**, *92*, 246401.
- [31] Klimeš, J.; Bowler, D. R.; Michaelides, A. Van der Waals density functionals applied to solids. *Phys. Rev. B* **2011**, *83*, 195131.
- [32] Gao, L.; Sun, J. T.; Lu, J. C.; Li, H.; Qian, K.; Zhang, S.; Zhang, Y. Y.; Qian, T.; Ding, H.; Lin, X. et al. Epitaxial growth of honeycomb monolayer CuSe with dirac nodal line fermions. *Adv. Mater.* **2018**, *30*, 1707055.
- [33] Shkvarin, A. S.; Yarmoshenko, Y. M.; Yablonskikh, M. V.; Merentsov, A. I.; Shkvarina, E. G.; Titov, A. A.; Zhukov, Y. M.; Titov, A. N. The electronic structure formation of Cu<sub>x</sub>TiSe<sub>2</sub> in a wide range (0.04 < x < 0.8) of copper concentration. *J. Chem. Phys.* **2016**, *144*, 074702.
- [34] Song, Z. P.; Yi, J. X.; Qi, J.; Zheng, Q.; Zhu, Z. L.; Tao, L.; Cao, Y.; Li, Y.; Gao, Z. Y.; Zhang, R. Z. et al. Line defects in monolayer TiSe<sub>2</sub> with adsorption of Pt atoms potentially enable excellent catalytic activity. *Nano Res.* **2022**, *15*, 4687–4692.
- [35] Moulder, J. F.; Stickle, W. F.; Sobol, P. E.; Bomben, K. D. *Handbook of X-ray photoelectron spectroscopy*; Physical Electronics: Eden Prairie, MN, USA, **1995**.



This is an open access article under the terms of the Creative Commons Attribution 4.0 International License (CC BY 4.0, <https://creativecommons.org/licenses/by/4.0/>).